CrossMark

ELSEVIER

http://dx.doi.org/10.1016/j.ultrasmedbio.2015.05.016

● *Original Contribution*

SINGLE-CAMERA CLOSED-FORM REAL-TIME NEEDLE TRACKING FOR ULTRASOUND-GUIDED NEEDLE INSERTION

Mohammad Najafi,* Purang Abolmaesumi,* and Robert Rohling*[†]

*Department of Electrical and Computer Engineering, University of British Columbia, Vancouver, British Columbia, Canada;
and [†]Department of Mechanical Engineering, University of British Columbia, Vancouver, British Columbia, Canada

Abstract—Many common needle intervention procedures are performed with ultrasound guidance because it is a flexible, cost-effective and widely available intra-operative imaging modality. In a needle insertion procedure with ultrasound guidance, real-time calculation and visualization of the needle trajectory can help to guide the choice of puncture site and needle angle to reach the target depicted in the ultrasound image. We found that it is feasible to calculate the needle trajectory with a single camera mounted directly on the ultrasound transducer by using the needle markings. Higher accuracy is achieved compared with other similar transducer-mounted needle trackers. We used an inexpensive, real-time and easy-to-use tracking method based on an automatic feature extraction algorithm and a closed-form method for pose estimation of the needle. The overall accuracy was 0.94 ± 0.46 mm. (E-mail: rohling@ece.ubc.ca)   © 2015 World Federation for Ultrasound in Medicine & Biology.

Key Words: Needle insertion, Needle tracking, Camera, Closed-form, Ultrasound, Guidance.

INTRODUCTION

The effectiveness of a treatment and the correctness of a diagnosis are often dependent on the accuracy of related percutaneous insertion. In procedures such as biopsy (*e.g.*, prostate, kidney, breast and liver), brachytherapy and anesthesia, millimeter-level placement accuracy is required. In some brain, fetus, eye and ear procedures, sub-millimeter placement accuracy is desirable (Abolhassani et al. 2007).

For instance, accurate needle-tip placement is a challenge in epidural needle insertion (Bernards et al. 2009), a central nerve block technique achieved by injection of a local anesthetic close to the spinal nerves (Anim-Somuah et al. 2005). Studies suggest that inappropriate needle position may occur in as many as 30% of lumbar epidural injection procedures performed with either the sacral hiatus or lumbar puncture approach and affects the outcome (Bartynski et al. 2005).

In many applications, the intervention can be aided with ultrasound guidance. However, conventional free-hand needle placement involves simultaneous manipulation of the ultrasound probe and needle while the physician mentally relates images on a video screen to locations inside the patient (Boctor et al. 2008). In fact, it is a challenge for the surgeon to visualize the needle trajectory inside the tissue just by looking at the ultrasound image and the needle. It is especially difficult to align the cross-sectional ultrasound plane with the needle tip at the desired spot in the tissue (Khosravi et al. 2007). The main challenge is to select the appropriate puncture site and needle orientation so that, on insertion, the needle tip follows the desired trajectory and hits the target in the image plane. Figure 1 depicts an example of an out-of-plane needle trajectory planning process.

In other words, visualization and hand–eye coordination skills of the surgeon play a major role in the success of this process. If the insertion fails because of either a wrong puncture site or a wrong needle trajectory, the needle misses the target, and re-insertion is required (Chan et al. 2005).

To improve the performance of needle insertion in an ultrasound-guided needle insertion procedure, it is helpful to track the pose of the needle with respect to the coordinate system of the ultrasound image. Therefore, the trajectory of the needle can be displayed on the image

Address correspondence to: Robert Rohling, Department of Electrical and Computer Engineering, University of British Columbia, 3059-2332 Main Mall Vancouver, BC, V6T 1Z4, Canada. E-mail: rohling@ece.ubc.ca
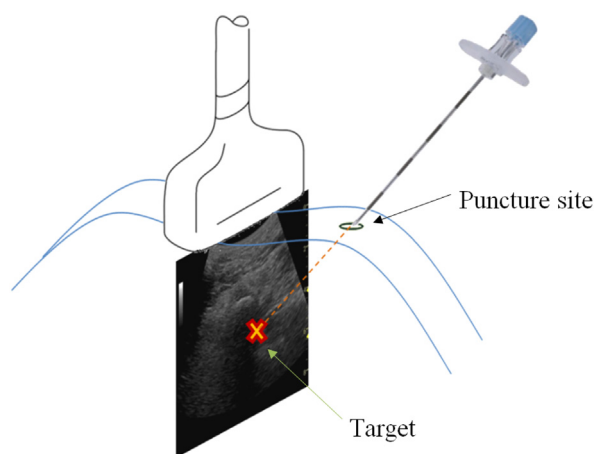
Fig. 1. Out-of-plane needle trajectory planning. The appropriate needle trajectory for the given puncture site on the skin and the selected target on the ultrasound image are represented by the *dashed line*.

in real time so that the proper trajectory can be chosen before the skin puncture (Fig. 1).

Tracking technique

There are different types of commercial systems for tracking needles, such as magnetic, mechanical and optical trackers. Most systems are designed to operate over a work space of several cubic meters so have an inherent trade-off between accuracy and work space. Magnetic trackers are commonly used, but are affected by nearby metallic objects and require a fixed-field generator, while mechanical guides and trackers limit the freedom of movement. Fixed camera-based optical trackers do not have these drawbacks, but require a line of sight between the tool and the cameras (usually mounted on a stand beside the subject) (Mercier et al. 2005), which is especially difficult for wall-mounted cameras.

Previous work had indicated that small stereo cameras can be mounted directly on the ultrasound transducer to allow better trade-offs between accuracy, work space, cost and line-of-sight issues (Chan et al. 2005; Khosravi et al. 2007). The key insight is that the work space of the needle relative to ultrasound is small so a trade-off of small work space can result in high accuracy of tracking.

Chan et al. (2005) worked on a method with two cameras mounted on a 2-D probe. They estimated the needle trajectory by observing the needle near the puncture site on the skin. They illustrated the feasibility of the technique, but found that the error of calibration (the intrinsic and extrinsic parameters) of the two cameras and the error of calibration of the ultrasound imaging plane and the probe are limiting factors. In fact, the errors in calibration of each step accumulate and lead

to a significant final error in needle trajectory estimation. They achieved an accuracy of 3.1 ± 1.8 mm.

Khosravi et al. (2007) also used stereo cameras for needle pose estimation, but tried to eliminate the need for several calibration steps by employing direct mapping from un-calibrated stereo images to needle position and orientation. They collected a set of needle poses and the corresponding 2-D positions in the images. Then a training algorithm was used to find the mapping between the images of the needle and its 3-D pose. They achieved an average error of 2.4 mm in position and 2.61° in orientation.

Wang et al. (2012) used a Kinect sensor (Zhang 2012) as a tracking tool for needle pose estimation and achieved an accuracy ranging from 2.6 ± 1.7 to 6.9 ± 5.1 mm. In a more recent work (Stolka et al. 2014b), a stereo camera system was used for needle pose estimation, and this tracking system was commercialized (Stolka et al. 2014a), confirming the interest in such camera-based trackers mounted on the ultrasound transducer. The accuracy of this system was 3.3 ± 2.3 mm.

A single camera would provide further improvements in cost, complexity and size. Therefore, a single camera system is proposed here. The main challenge expected in tracking with a single camera is that the pose of the needle is less accurately measured in the range direction, but this limitation can be mitigated by exploiting the known markings on the needle. The key idea in our proposed method is to exploit the regular markings that appear on many medical needles (*e.g.*, epidural needles) at known intervals (*e.g.*, 1 cm) for tracking.

Single-camera pose estimation

Single-camera pose estimation methods can be categorized into two approaches. First are feature-based training methods that employ registered labels in a database to find the position of the camera based on the comparison between captured features and the database. Second are mathematical–geometrical methods, which employ geometrical relations between captured images and the camera position to determine the position and orientation of the camera (Rahbar and Pourreza 2008).

In feature-based methods, a feature detector is used to extract features from each image to be compared with the feature database. For instance, Collet et al (2009) have used scale invariant feature transform (SIFT) (Lowe 2004) features to extract local descriptors from images in their system for object pose estimation. However, images of a needle normally do not have enough texture to produce enough SIFT features for accurate pose estimation. Moreover, issues such as variable light reflectance on the metallic surfaces of a needle can make correct feature extraction and mapping more difficult. Moreover, although feature-based methods are fast, the

pose estimation accuracy is limited to the size of the training database (Rahbar and Pourreza 2008).

On the other hand, mathematical–geometrical methods are not constrained to a training data set. Their accuracy is typically determined by the feature extraction step and the camera's intrinsic calibration accuracy. Mathematical–geometrical methods fall into two categories: analytic closed-form and iterative optimization methods.

Analytic closed-form methods provide an analytical solution to the needle's/object's pose based on the geometrical properties of the model and the corresponding features extracted from the image. The main advantage of these methods is their low computational cost, which makes them suitable candidates for real-time applications. Examples include three-point perspective pose estimation (Haralick et al. 1991), pose estimation using 2-D to 3-D corner correspondence (Shi et al. 2004) and pose estimation from metric rectification of co-planar points (Lucchese 2006). A novel mathematical–geometrical formulation is devised here for needle trajectory calculation using the centimeter-spaced black markings on many needles, such as standard epidural needles.

In the iterative optimization methods, the needle's/object's pose is estimated by optimization of a geometric constraint, either in the 3-D world coordinates or in the image coordinates. These methods can be less sensitive to feature extraction error because they usually use a large number of features, but are more computationally expensive. Moreover, non-linear optimization methods rely on a good initial guess to converge to the correct solution.

One advantage of a closed-form mathematical–geometrical solution is that it is possible to optimize the system design by calculating the sensitivity of each of the parameters in the pose estimation procedure using the known error propagation model. For instance, in one study (Luhmann 2009) on pose estimation of a planar object relative to a fixed reference, the effects of several parameters on the 6-*df* (degrees of freedom: 3 translation and 3 rotation) pose parameters were investigated using a Monte-Carlo simulation. It was concluded that the distance between the camera and the object, and hence the average image scale, plays the most important role in calculating accuracy in the viewing direction. In addition, the size of the object, that is, the spatial distribution of reference points, is the second most important design parameter. Moreover, among all 6-*df* parameters, translation in Z (optical axis) direction and rotations around X and Y (pitch and yaw) are the most sensitive. In the case of focal length variation (while adjusting the viewing distance to keep image scale constant), the precision in Z translation and pitch and yaw rotations decreases linearly with increasing focal length, which is to be expected from

the known advantage of wide-angle lenses for orientation purposes. Object tilt (around X or Y) up to 50° almost does not affect the parameters. These findings were used in our proposed design discussed in this article.

For the needle tracking problem, the markings are collinear and the needle trajectory is a line that can be described by 5 *df* (excluding the rotation around the needle's axis). Although there are closed-form solutions for planar (2-D) objects for 6-D pose estimation (Collet et al. 2009; Rahbar and Pourreza 2008), to the best of our knowledge, we are the first to propose a closed-form method for estimation of the pose of a linear object using a single image of a camera.

In our previous work (Najafi and Rohling 2011), we reported the feasibility of such a system. We have substantially improved our previous work in terms of accuracy (3.0 ± 2.6 mm), robustness and flexibility. Here, a more generalized version of the closed-form solution, which can account for a variable number of feature points, is presented. In addition, the feature extraction algorithm has been improved. Moreover, rotation or dismounting of the camera no longer requires ultrasound recalibration. This was made possible by using a fixed marker on the transducer and using a mirror to calibrate the camera with respect to that marker at the time of construction/assembly. Our multiwedge calibration method, which is a more accurate ultrasound calibration method (Najafi et al. 2014), was also employed here. The precision and accuracy of the needle estimation were measured relative to the camera, as was the accuracy of the overall ultrasound guidance system. The emphasis is on out-of-plane needle insertions, but the method could be converted to in-plane needle insertion by remounting the camera on the side of the transducer.

METHODS

A SonixTOUCH ultrasound machine (Ultrasonix Medical, Richmond, BC, Canada) was used for ultrasound imaging. An L14-5 transducer with 7.2-MHz center frequency was used for ultrasound imaging.

The camera was an FL2G-13S2M-C (Point Grey Research, Richmond, BC, Canada) with a DF6HA-1B lens (Fujifilm Group, Fujinon, Saitama, Japan). The camera had a mono 1.3-MP Sony ICX204 CCD, 1/3-in., 4.65-μm sensor. The frame rate was 30 FPS and the image size was 1,288 × 964 pixels. The lens had a 6-mm focal length, iris range of F1.2 to F–16 and horizontal and vertical field angles of 56°09′ and 43°36′, respectively.

Mathematical framework

A standard camera model was adopted here. The principal point (x_p, y_p), the effective focal length (f_x, f_y) and the lens distortion parameters were determined from a separate

standard calibration process explained below. Effective focal length and principle point are measured in pixels. The skew coefficient defines the angle between the x and y pixel axes. The image distortion coefficients (radial and tangential distortions) are used to undistort the image.

As described earlier, the marking edge points of the needle $(Q = (Q_x, Q_y))$ were then used as the features required to extract the needle's pose (Fig. 2).

By use of the standard camera model (Lucchese 2006), it is possible to find the projection of any 3-D point $(P = (P_x, P_y, P_z))$ in the camera plane:

$$\begin{bmatrix} Q_x \\ Q_y \end{bmatrix} = \begin{bmatrix} f_x \dfrac{P_x}{P_z} + x_p \\ f_y \dfrac{P_y}{P_z} + y_p \end{bmatrix} \tag{1}$$

where f_x and f_y define the effective focal lengths of the camera along the two axes.

The markings on the needle reside on a straight line, and based on the model described earlier, it is obvious that their projection points on the camera plane are also collinear. Moreover, all the marking points, their projections and the focal point are in the same plane (Fig. 3).

The feature extraction procedure, described in the next section, finds the projected points (Q_i) in the image, and $F = (x_p, y_p, f)$ is calculated in the camera calibration procedure. Actual marker distances, $d_i = \|P_{i+1} - P_i\|$, are assumed to be known. For an epidural needle, in particular, the marking distances are all equal $(d_i = 1 \text{ cm})$. However, the proposed method is not limited to the equal spacing constraint and can be generalized for needles with non-equal marking spacings.

Having the projection points (Q_i), we can define unit vectors $\vec{V_i}$ as

$$\vec{V_i} = \frac{Q_i - F}{\|Q_i - F\|}. \tag{2}$$

Any of P_i points can be described as

$$P_i = s_i \vec{V_i} + F \tag{3}$$

We also define vectors G_i as

$$\vec{G_i} = P_{i+1} - P_i \tag{4}$$

and as mentioned earlier, $\left\|\vec{G_i}\right\| = d_i$ are known. Therefore,

$$\frac{s_{i+1} \vec{V_{i+1}} - s_i \vec{V_i}}{d_i} = \frac{\vec{G_i}}{\left\|\vec{G_i}\right\|}, \tag{5}$$

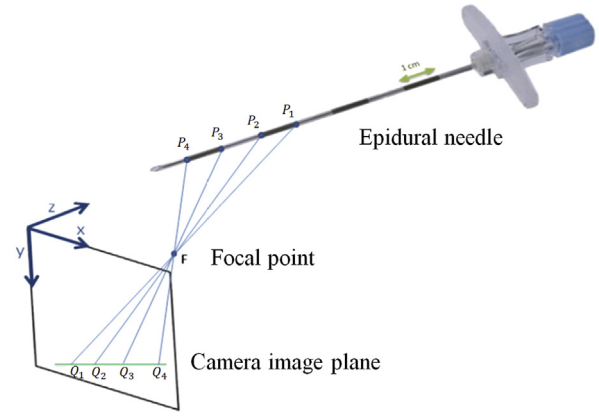where s_i are unknown and to be determined, and the right-hand side is always a unit vector defined as

Fig. 2. Epidural needle with 1-cm markings is projected into the camera plane using the standard camera model.

$$\vec{U} = \frac{\vec{G_i}}{\left\|\vec{G_i}\right\|} \tag{6}$$

All the $\vec{V_i}$ vectors reside on the same plane with a normal vector, $\vec{n}$:

$$\vec{n} = \frac{\vec{V_i} \times \vec{V_j}}{\left\|\vec{V_i} \times \vec{V_j}\right\|}, \ \forall i \neq j \tag{7}$$

Therefore, we can describe $\vec{V_i}$ as a linear combination of two perpendicular vectors. Without loss of generality, we define $\vec{A} = \vec{V_1}$ and $\vec{B}$ as

$$\vec{B} = \vec{n} \times \vec{A} \tag{8}$$

and hence we can describe $\vec{V_i}$ as
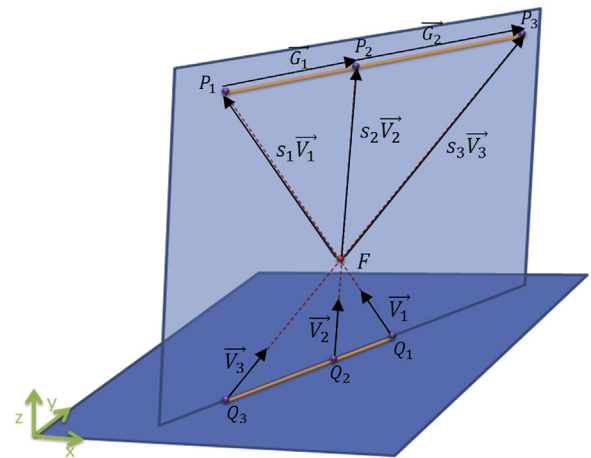
$$\vec{V_i} = \alpha_i \vec{A} + \beta_i \vec{B} \tag{9}$$

Fig. 3. Three known collinear points on the object (P_1, P_2 and P_3), the corresponding projections on the camera plane (Q_1, Q_2 and Q_3) and the focal point (F) all reside on the same plane.

where α_i and β_i coefficients are calculated from

$$\alpha_i = \overrightarrow{V_i} \cdot \overrightarrow{A}, \quad \beta_i = \overrightarrow{V_i} \cdot \overrightarrow{B} \qquad (10)$$

Now we can substitute $\overrightarrow{V_i}$ in (5) with (9):

$$\frac{s_{i+1}\left(\alpha_{i+1}\overrightarrow{A}+\beta_{i+1}\overrightarrow{B}\right)-s_i\left(\alpha_i\overrightarrow{A}+\beta_i\overrightarrow{B}\right)}{d_i} = \overrightarrow{U} \qquad (11)$$

We can write (11) for $j \neq i$ and subtract:

$$\frac{s_{i+1}\left(\alpha_{i+1}\overrightarrow{A}+\beta_{i+1}\overrightarrow{B}\right)-s_i\left(\alpha_i\overrightarrow{A}+\beta_i\overrightarrow{B}\right)}{d_i} - \frac{s_{j+1}\left(\alpha_{j+1}\overrightarrow{A}+\beta_{j+1}\overrightarrow{B}\right)-s_j\left(\alpha_j\overrightarrow{A}+\beta_j\overrightarrow{B}\right)}{d_j} = 0 \qquad (12)$$

By rearranging eqn (12), we have

$$\overrightarrow{A}\left[d_j(s_{i+1}\alpha_{i+1}-s_i\alpha_i)-d_i(s_{j+1}\alpha_{j+1}-s_j\alpha_j)\right] \\ + \overrightarrow{B}\left[d_j(s_{i+1}\beta_{i+1}-s_i\beta_i)-d_i(s_{j+1}\beta_{j+1}-s_j\beta_j)\right] = 0. \qquad (13)$$

Because $\overrightarrow{A}$ is perpendicular to $\overrightarrow{B}$, their linear combination can be only zero when both coefficients are also zero. Therefore, after rearrangement, we have

$$s_{j+1}\left(d_i\alpha_{j+1}\right)+s_j\left(-d_i\alpha_j\right)+s_{i+1}\left(-d_j\alpha_{i+1}\right)+s_i\left(d_j\alpha_i\right) = 0 \qquad (14)$$

and

$$s_{j+1}\left(d_i\beta_{j+1}\right)+s_j\left(-d_i\beta_j\right)+s_{i+1}\left(-d_j\beta_{i+1}\right)+s_i\left(d_j\beta_i\right) = 0 \qquad (15)$$

So far, we have derived the necessary equations (14, 15) to solve for the unknowns (s_i). These equations are a linear function of unknowns and can be written for any pair of $i \neq j$ values. If we have p points, we can write independent equations for $i = 1$ to $p-1$ and $j = i+1$ to $p-1$. So if we define the matrix form of the problem as

$$C_{q \times p} S_{p \times 1} = [0]_{q \times 1} \qquad (16)$$

where $S_{p \times 1} = [s_1 \ldots s_p]^t$ is the vector of unknowns, and $q = (p-1)(p-2)$ is the number of equations. The C matrix can be formed, for example, by using (14) for the even rows and using (15) for the odd rows. Depending on the values of i and j, the rth row of C can be written as follows: if $j = i+1$ and r is even, then the non-zero elements of this row are

$$\left[c_{ri}, c_{rj}, c_{r(j+1)}\right] = \left[d_j\alpha_i, -d_i\alpha_j-d_j\alpha_{i+1}, d_i\alpha_{j+1}\right] \qquad (17)$$

else, if $i = j+1$, and r is even:

$$\left[c_{r(i+1)}, c_{rj}, c_{r(j+1)}\right] = \left[-d_j\alpha_{i+1}, d_i\alpha_j, d_j\alpha_i+d_i\alpha_{j+1}\right], \qquad (18)$$

else

$$\left[c_{ri}, c_{r(i+1)}, c_{rj}, c_{r(j+1)}\right] = \left[d_j\alpha_i, -d_j\alpha_{i+1}, -d_i\alpha_j, d_i\alpha_{j+1}\right] \qquad (19)$$

Note that the rest of the elements in each row are zero. Equation (15) should be used for odd r values and equations similar to (17), (18) and (19) can be written, except that α should be replaced with β.

Finally, to find the solution, we know that (16) is a linear system of equations with a zero right-hand side. Therefore, the null space gives a solution for S. The unique solution is obtained when the distance constraint

$$\left\| s_i\overrightarrow{V_i} - s_{i+1}\overrightarrow{V_{i+1}} \right\| = d_i \qquad (20)$$

is applied, which means that the calculated S should be scaled as

$$\widehat{S} = S \frac{d_i}{\left\| s_i\overrightarrow{V_i} - s_{i+1}\overrightarrow{V_{i+1}} \right\|} \qquad (21)$$

Now by using $\widehat{S}$, we may now calculate P_i using (3) and G_i using (4) and, hence, determine the pose of the needle. Note that at least three marking points are required to solve for all the unknowns.

Automatic feature extraction

To estimate the pose of the needle, marking edge points should be extracted from each image of the needle. These edge points are defined as the intersection of the centerline of the needle with the marking edge lines (Fig. 4a). The accuracy of the pose estimation is directly related to the accuracy of this segmentation procedure.

One classic approach is to identify the needle in the image using the Hough transform (Gonzalez et al. 2004). Although several practical issues limit the accuracy of this approach, it can be used to find the approximate location of the needle. One of the challenges is that in a practical interventional procedure, there may be many objects
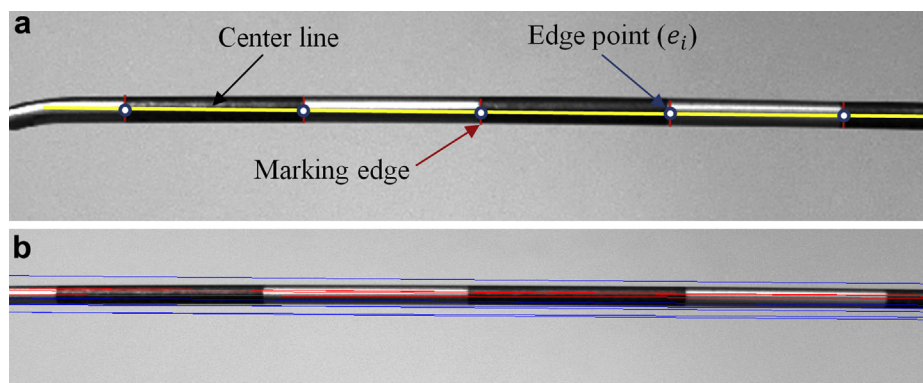
Fig. 4. (a) Edge points should be extracted from the image of the needle. Centerline: marking edges and edge points are shown. (b) Examples of "off-the-needle" lines (in *blue*) and "on-the-needle" lines (in *red*).

in the background with strong edges similar to a needle that can interfere with proper recognition of the needle using the Hough transform. Second, the variable specular light reflections on the metallic surface of the needle can produce misleading strong edges. Moreover, because the needle can be fairly close to the camera, its two border lines may not appear as parallel lines in the image because of perspective viewing. Also, the marking edges may appear as curved lines because of the cylindrical shape of the needle. Therefore, a simple Hough transform cannot always accurately recognize the needle and its centerline. It should be emphasized that correct detection of the needle is needed, together with an accurate estimate of the centerline of the needle, for accurate detection of the marking edge points.

Therefore, we adopted a novel approach by considering the fact that the most distinctive feature of such a marking system is the consecutive black and white pattern on the needle. Hence, for any arbitrary line in the image, when considering the pixel values along the line, if the line lies on the needle, then significant steps occur at the marking edges. The pixel values will rise to a higher level when the transition is from black to white regions, and there will be a sudden drop in values when going from white to black regions. This gives one criterion to identify whether the chosen line lies on the needle or not. Figure 4b illustrates an example of "off-

the-needle" lines (in blue) and "on-the-needle" lines (in *red*).

In our proposed method, instead of detecting the needle's centerline first, we collect various points that reside on the marking edges (Fig. 5). Then these points are grouped into different classes using a clustering technique. Each class, in fact, represents a collection of the points residing at each marking edge of the needle. The center of each cluster is calculated, and a line is fitted to all the center points. This line is considered as a more accurate estimate of the needle's centerline. Finally, to fine-tune the segmentation results, the marking edges are recalculated by running an edge detection algorithm along this estimated centerline.

Collecting marking edge points

We start with an overview of the procedure. The algorithm starts with an initial estimate for the needle centerline. The estimate can come from the previous frame, if the current frame is not the first frame. For the first frame, the estimate is provided by the Hough transform (using the Canny edge detector). Then, random lines are generated around this estimate by adding random variables to the slope and line intercept. Pixel values on each line are examined to determine if it is an "on-the-needle" line. In that case, the intersection points of the line with the marking edges will be stored.
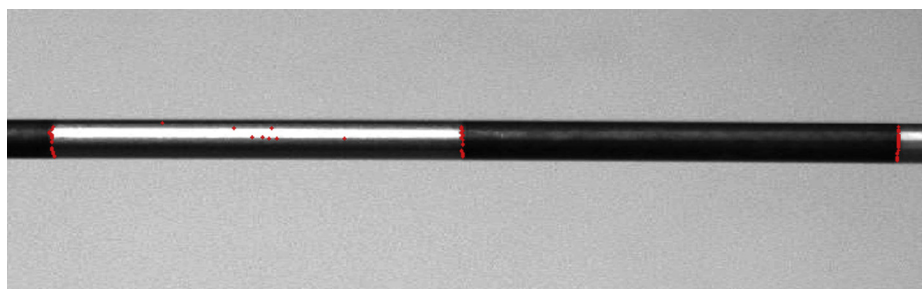

Fig. 5. Points associated with the peak values on each line are stored (*red dots*). These points are clustered to find marking edges.

To detect an "on-the-needle" line, the edges of the pixel values along the line were detected to determine whether a pattern of consecutive rising and falling edges can be observed. For edge detection, first the derivative of the pixel values was calculated using a smooth noise-robust differentiator (Holoborodko 2008) ($N = 9$), as illustrated in Figure 6. Next, peaks that exceeded a certain threshold (minpeakheight) and had indices separated by more than minpeakdistance and with peak values exceeding their neighbors by greater than threshold were identified. This can be performed by finding the zero crossings of the first derivative and taking only those that meet the mentioned conditions. Here, we used the findpeaks() function in MATLAB (The MathWorks, Natick, MA, USA). Proper values for these parameters should be chosen based on the experimental setup. Specifically, minpeakdistance is related to the length of the markings in pixels and, therefore, depends on the image resolution, lens field of view and distance of the needle to the camera. Table 1 lists the parameters used in our experiments.

Then the sign (rising or falling edge) of the peak values was determined, and the number of consecutive positive and negative peaks was measured. If this number was greater than 75% of the total number of detected peaks on that line, then this line was considered as an "on-the-needle" line. If that was the case, then the points associated with the peak values on the line were stored. Higher threshold values ($>75\%$) will reject more candidate lines, whereas lower values will allow a wider range of candidate lines. The method, however, is not sensitive to this threshold value, because as described in the next section, the edge points will be clustered and outlier points would be removed.

Sometimes a cluttered background can be misleading and could result in wrong estimation of the needle centerline when using the Hough transform. This can be verified if the percentage of "on-the-needle" lines is very small ($<10\%$). In that case, the edge detection parameters prior to applying the Hough transform should be altered or the algorithm can run without an initial guess with a wide search range (*e.g.*, random search).

Clustering edge points

The aforementioned criteria do not guarantee that any "on-the-needle" line is always on the needle and they do not guarantee that all the detected peak points are on the marking edges (Fig. 5). However, statistically, the majority of these points will be on the marking edges, and therefore, it is possible to find the actual marking edges by clustering them. The clustering procedure should find clusters of points with low interclass distance and high intraclass distance.

Hierarchical clustering (Hastie et al. 2009) was used here to cluster the points. In hierarchical clustering, data are grouped over a variety of scales by creating a cluster tree or dendrogram. The tree is not a single set of clusters, but rather a multilevel hierarchy, where clusters at one level are joined as clusters at the next level. This allows us to decide the level or scale of clustering that is most appropriate for one application. The cluster() function in MATLAB was used with cutoff = c and along with distance criterion as an option, which uses the distance between the two subnodes merged at a node to measure node height. All leaves at or below a node with height less than c were grouped into a cluster. In Figure 7 is the dendrogram of the clustered points and the cutoff line ($c = 15$) used here. This value was chosen based on the average distance between markings with our experimental setup.

The number of points in each cluster was examined, and those including points less than 25% of the number of points in the biggest cluster were eliminated.
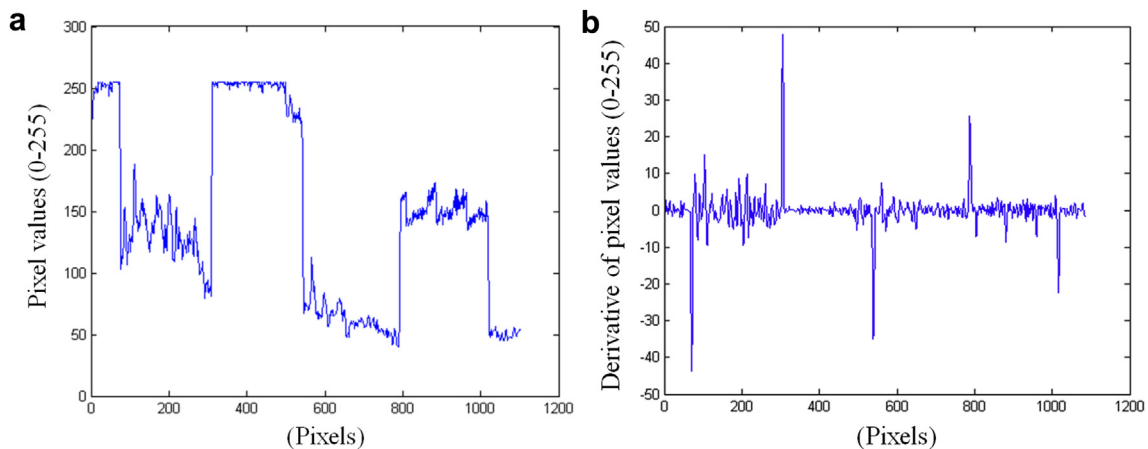

Fig. 6. (a) Pixel values along an "on-the-needle" line. (b) Derivative of the values using the smooth noise-robust differentiator.

Table 1. Parameters used in the automatic feature extraction algorithm

Parameter	Value	Unit
minpeakdistance	200	pixel
minpeakheight	5	—
Threshold	0.1	—
Cutoff	15	—

Finding the centerline and fine-tuning

In this stage, the center of each cluster was found first by fitting a second-order polynomial to the points in each cluster and removing the outliers. After refitting another polynomial to the remaining points, the center of the polynomial was chosen as the cluster's center point. Eventually, the centerline of the needle was calculated by fitting a line to these cluster center points.

Now, another step was taken for accurate estimation of the edge points, Q_i. The derivative of pixel values along the lines parallel to the calculated centerline was taken, and the peaks were detected. Then eventually, at each edge, the peak points were averaged in a weighted-average manner to find the edge points. Figure 8 illustrates the final results.

System calibration

To estimate the pose of the needle relative to the ultrasound image, we need to find the transformation from the camera's coordinate system to the ultrasound image coordinate system. This procedure is called *ultrasound calibration*. Also, the intrinsic parameters of the camera should be calibrated for the needle pose estimation procedure, as explained above.

One practical challenge is that the camera-to-ultrasound calibration should be performed every time the camera is mounted on the transducer. Also, this limits the range of rotation of the camera that can be used. For example, the camera should be rotated 90° to perform an

Fig. 7. Dendrogram of the clustered points and the cutoff threshold of $c = 15$ (*red line*).

in-plane insertion as opposed to an out-of-plane insertion procedure.

To tackle this problem, we have proposed attaching a fixed checkerboard pattern to the transducer. The ultrasound calibration should be performed only once to find the transformation from the ultrasound image to the checkerboard pattern on the transducer, $^{T}T_{I}$. Then, each time the camera is remounted or has been rotated, only the transformation from the camera to the transducer's marker, $^{T}C_{I}$, needs to be calculated using a mirror. Figure 9 illustrates the coordinate systems of the transducer, the camera and the ultrasound image.

By placing a mirror in different poses and obtaining one image of the calibration pattern in each pose while keeping the camera and a checkerboard pattern fixed, it is possible to estimate the pose of the checkerboard pattern as well as all the mirror's poses (Kumar et al. 2008). An alternative approach is to attach another checkerboard pattern to a visible part of the mirror so that the pose of the mirror can be estimated directly from one image. The pose of the mirrored checkerboard pattern (on the transducer) can also be estimated. Eventually, the estimated pose should be mirrored back using the estimated mirror's plane to find the actual pose of the checkerboard pattern on the transducer. The width of the mirror should be taken into account in this procedure. We found that the former method is less robust compared with the latter, and hence, the latter was used here with a 5 × 5-mm, 6 × 8 checkerboard pattern on the mirror and a 10 × 10-mm, 5 × 5 checkerboard pattern on the transducer.

Ultrasound calibration

The transformation from the ultrasound image to the checkerboard pattern on the transducer, $^{I}T_{T}$, was estimated by ultrasound calibration. In our earlier work, we proposed a closed-form differential formulation based on a multiwedge phantom comprising five planes (Najafi et al. 2014). That method was used here for ultrasound calibration.

Camera calibration

Camera calibration was performed using a method developed based on Bouguet (1999). This method uses several images of a checkerboard pattern to estimate the camera's intrinsic parameters such as focal length, principal point and lens distortions. It can also estimate the pose of a checkerboard pattern with respect to the camera's coordinate system.

EXPERIMENTS AND RESULTS

Camera calibration

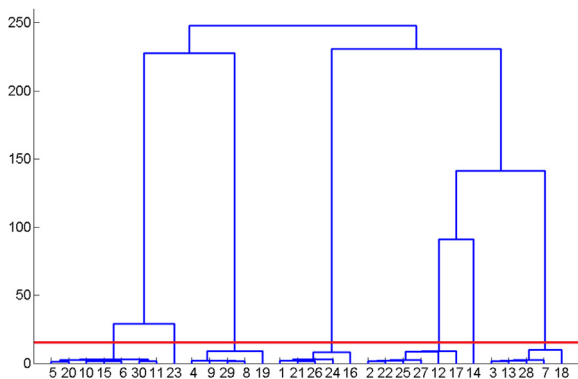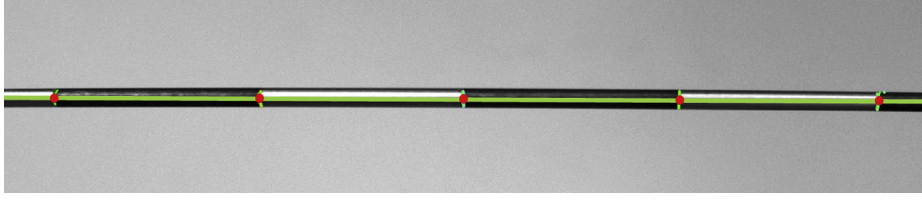Camera calibration was performed using 20 images of a checkerboard pattern by running the camera

Fig. 8. Final feature extraction results indicating the centerline (*green line*) and the marking edge centers (*red dots*).

calibration toolbox (Bouguet 1999). Table 2 summarizes the results showing the intrinsic parameters of the camera.

Precision of the feature extraction

In this section, first we investigate the effect of parameter selection on the feature extraction algorithm. For this purpose, the algorithm was applied to the same image of a needle 100 times, and the variability of the extracted edge points was measured by calculating the root mean square of the difference between the extracted edge points and their average.

Then the repeatability of the pose estimation algorithm was evaluated by using the extracted features and the camera's intrinsic parameters from the camera cali-bration. In the pose estimation results, the equation of the 3-D line of the needle is described with one point in space, P_i, and a unit direction vector, G_i. Here, the standard deviation of P_i was measured, as was the root mean square of the angle between G_i and their average, $\overline{G} = \frac{\sum_{i=0}^{100} G_i}{100}$. Table 3 summarizes the results, which indicate that the segmentation algorithm converges to a solution with a small variation that is due to errors in the segmentation procedure.

To measure the precision of the segmentation method, the automatic segmentation results were compared with the manual segmentation of the edge points, and the errors were evaluated. For this reason, 50 images of the needle in various positions were segmented manually and compared with the automatically segmented points in the images. A root mean square error of 2.2 pixels was calculated over 251 edge points.

Note that manual segmentation error also contributes to this measured error. Therefore, we have, in fact, measured an upper bound for the segmentation error.

Precision of the needle pose estimation

To measure the precision of the pose estimation method, the tip of the needle was fixed at a pivot point, and the needle was rotated in a circular motion. The needle was rotated continuously in a full 360° circle. Fifty frames were selected, and the pose of the needle was estimated for these frames. Obviously for a small tilt angle, low tip error will be expected and hence here, the needle was tilted as much as possible while trying to keep it in the field of view of the camera. The tilt angle was measured as the root mean squared angle between the estimated lines and their average, which was 14.8°.

The pivot point was estimated using a least-squares method by minimizing the distance from this point to all of the estimated lines. The root mean squared error for the pivot point was 0.41 mm.

This test measures the precision of the needle pose estimation in the camera's coordinate system. A precision test with only linear translations for the needle would not be as effective as this test. The reason is that in linear translation, the shape of the needle in the image does not significantly change compared with when it is placed
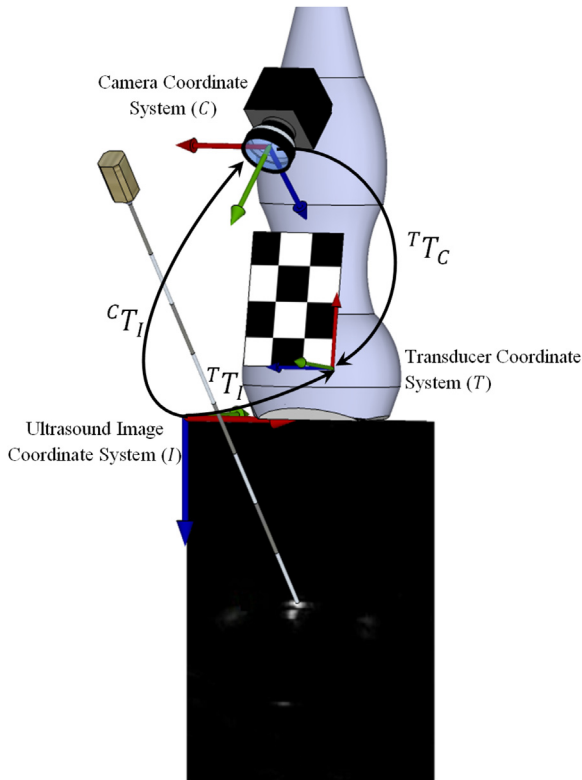

Fig. 9. Coordinate systems of the transducer, the camera and the ultrasound image.

Table 2. Camera intrinsic parameters obtained by camera calibration

Effective focal length	$[f_x, f_y] = [1672.90, 1654.61] \pm [5.62, 5.67] pixels$
Principle point	$[x_p, y_p] = [679.87, 505.27] \pm [4.98, 4.53] pixels$
Skew coefficient	$\alpha_c = [0.00] \pm [0.00]\ degrees$
Distortion	$k_c = [-0.231, 0.107, -0.001, 0.000, 0.000] \pm [0.011, 0.070, 0.000, 0.000, 0.000]$

in different orientations (especially in the depth direction). In this test we measure the tip position, which is more challenging because of the lever arm effect. Therefore, we conclude that our proposed test is a suitable indication of the precision for our pose estimation algorithm. However, this test does not measure the accuracy of the pose estimation.

Accuracy of the needle pose estimation

The accuracy of the needle pose estimation method (in camera's coordinate system) was measured by placing the tip of the needle on a grid of known positions and comparing them with the estimated tip position. For this reason, a testing device was manufactured with an Objet30 desktop 3D printer (Objet, Billerica, MA, USA with a printing tolerance of 28 μm). As illustrated in Figure 10, this testing device comprises a base with a grid of semispherical holes on its surface and a marker plane. The spacing of the grid points was 10 mm in both directions, and the radius of the semispheres was 0.25 mm. The marker plane is a flat piece with a checkerboard pattern attached to its top surface.

For the accuracy test, first the marker plane was placed inside the base and the camera captured one image of it. The pose of the marker plane was estimated from the checkerboard pattern, and therefore, the location of the grid points was calculated (in the camera's coordinate system). Then the marker plane was removed (without moving the base) and the needle's tip was placed in each of the holes (4 × 5 points). For each hole, the pose of the needle was estimated using the proposed method, and the estimated tip point was compared with its actual position. The root mean squared error was 0.49 mm.

The needle was manually placed at each grid point. The average angle between the needle and the grid plane was 59.0°, and the average angle between the needle and the camera image plane was 19.6°. The angle between the

Table 3. Measurement of repeatability of the feature extraction and pose estimation algorithms

Feature extraction error	$RMS(e_x, e_y) = [0.11, 0.7]$ pixels
3-D point estimation error	$std(P_i) = [0.008, 0.031, 0.031]$ mm
Direction estimation error	$RMS(\arccos(G_i \cdot \overline{G}/\|\overline{G}\|)) = 0.09°$

optical axis of the camera and the ultrasound image plane was 24.9°.

Overall system accuracy

The primary goal of the proposed system is to estimate the intersection of the needle with the ultrasound image so that the proper needle trajectory to hit a specific target on the ultrasound image can be chosen prior to skin puncture.

To measure the accuracy of the overall system, an out-of-plane needle insertion experiment was performed in a water bath. The needle was partially immersed in water so that the intersection of the ultrasound plane with the needle could be seen as a point in the ultrasound image. Part of the needle that was out of the water was visible with the camera and was used for estimating the pose of the needle. A 20-cm-long needle was used for this experiment.

By use of a linear stage, the needle was moved in 2-mm steps laterally at approximately 10- and 20-mm axial depths (26 points in total), as illustrated in Figure 11a. The tilt angle of the needle, the angle between the needle and the ultrasound image plane, was approximately 42°, and the angle between the needle and the optical axis of the camera was about 67°. The average angle between the needle and the camera image plane was 26.9°.

Ultrasound images were segmented manually by clicking on the center of the needle's intersection, which would appear as a cloud of pixels. These segmented target points were compared with the estimated intersection points (Fig. 11b). The mean and standard deviation of the distance error were 0.94 and 0.46 mm, respectively.

Sensitivity analysis of the needle pose estimation

To measure the effect of various parameters such as depth, needle tilt angle, needle yaw angle and number of edge points on accuracy, a sensitivity analysis test was performed by simulating the pose estimation process. The mathematical formulation of the system and the standard camera model was used with a noise source model as input. As discussed under Precision of the Feature Extraction, the root mean squared segmentation error was measured as 2.2 pixels, and hence, here, the noise was modeled as a normal random variable with a standard
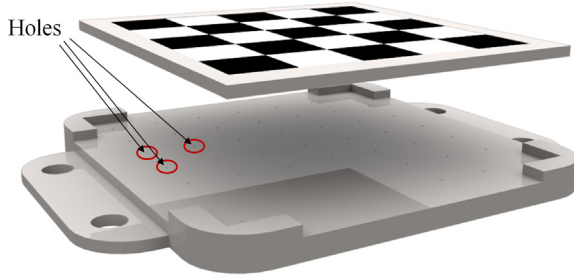
Fig. 10. Accuracy testing device composed of a base with a grid of semispherical holes on its surface and a marker plane. The marker plane is a flat piece with a checkerboard pattern attached to its top surface.

deviation of 2.5 pixels ($\sigma_x = \sigma_y = 2.5$). For the base case, the needle's pose and the other parameters were chosen similar to those in the Overall System Accuracy section. The angle between the needle and the ultrasound image plane was 45°, the intersection depth was 20 mm and three edge points were used.

In the first scenario, the intersection depth was varied from 10 to 50 mm to evaluate its effect on the accuracy of the pose estimation method. Figure 12a illustrates the root mean square of the estimation error at different depths and indicates that the error slowly increases at greater depths.

In the second scenario, the needle's tilt angle, the angle between the needle and the axial axis of the imaging plane, was varied from 15° to 65°. Note that the angle between the optical axis of the camera and the ultrasound image plane was approximately 25°. Therefore, this range of angles corresponds to the range of 40° to 90° for the angle between the needle and the optical axis of the camera. The estimation error is expected to be minimum when the needle is parallel to the camera image plane (needle is perpendicular to the optical axis of the camera). As can be seen in Figure 12b, the lowest error is observed at the needle tilt angle of 65°, which corresponds to such case.

Next, the effect of the yaw rotation of the needle (rotation around the axial axis of the ultrasound image) was considered. The yaw angle was varied from −30° to 30° and its effect on the accuracy of the method was evaluated. As illustrated in Figure 12c, fairly small variation is observed on the estimation error by varying this parameter.

Finally, the number of edge points was varied from 3 to 7 to investigate if using more edge points increases the accuracy because of the averaging effect. Results illustrated in Figure 12d confirm that the estimation error decreases by using more edge points.

The overall accuracy of the system is also influenced by the calibration accuracy. To investigate this, instead of adding a segmentation error, a constant error was added to the calibration parameters. An error of 1° was added to any of the rotation parameters (α, β, γ) each time. The estimation error (caused by this calibration error) was evaluated for different target depths (Fig. 12e). It can be seen that the error in β, rotation around the y-axis of the camera, has the largest impact on the accuracy of this system. The error increases with depth and can reach up to 1 mm at the depth of 60 mm. An error in translation parameters of calibration would affect the estimation accuracy in direct proportion to its size.

Real-time implementation

The algorithm was implemented in both MATLAB and C++. In the C++ implementation, the OpenCV library was used, and the overall method runs in real time (50 ms) on a standard computer workstation with a Core 2 Duo CPU at 2.93 GHz and 4 GB of RAM.
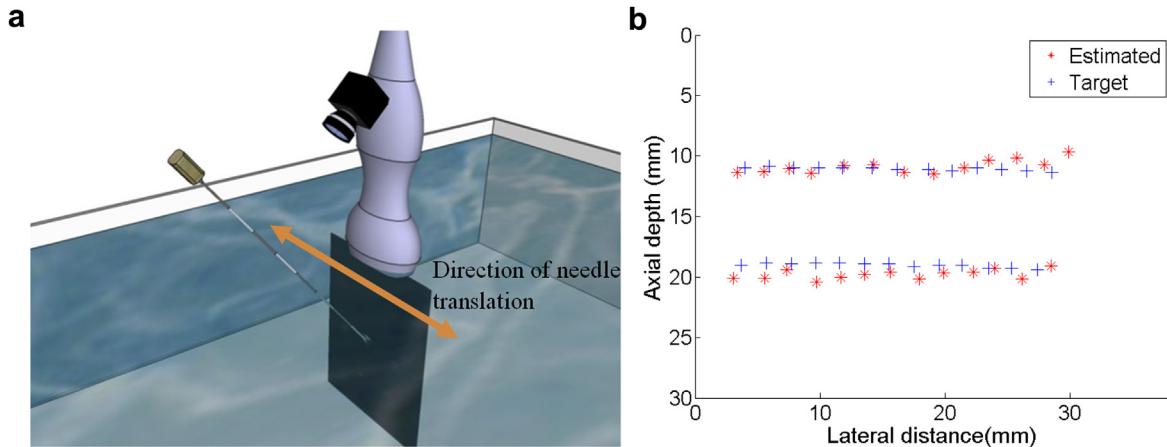

Fig. 11. (a) Schematic of the accuracy test experiment and depiction of needle movement. (b) Segmented target points have been compared with the estimated intersection points.
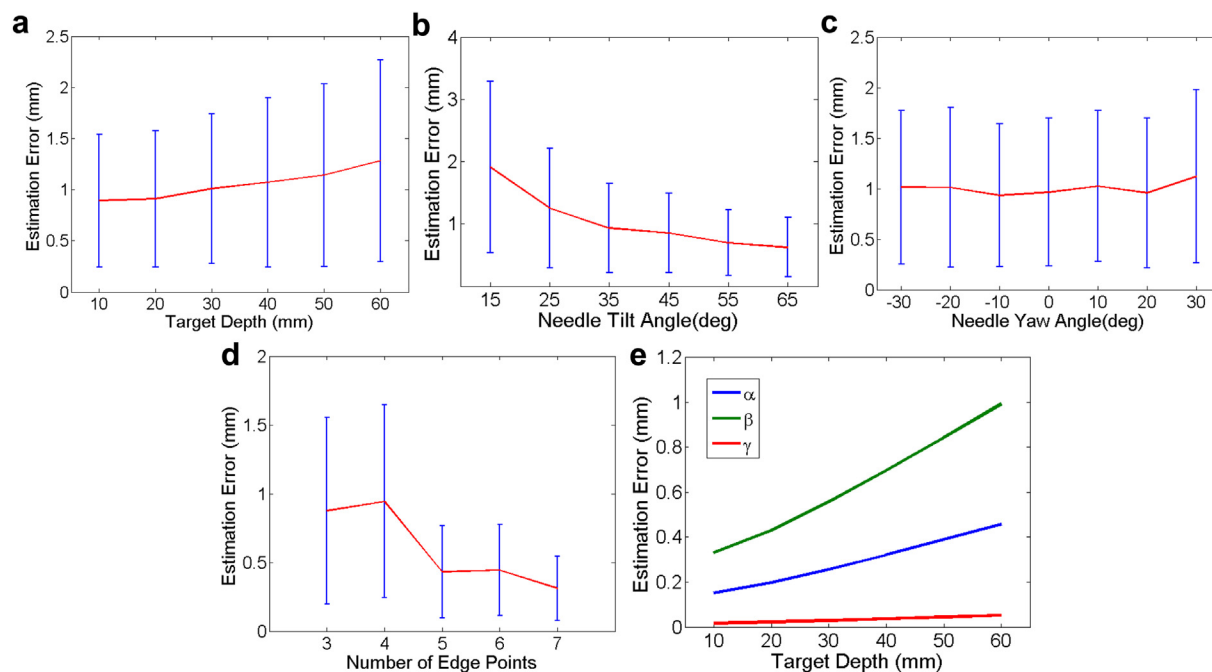
Fig. 12. Results of the sensitivity analysis test in various scenarios created by (a) varying the target depth, (b) varying the tilt angle, (c) varying the yaw angle, (d) using different numbers of edge points and (e) evaluating the effect of error in rotation parameters of the calibration matrix on the overall estimation error.

DISCUSSION

Under Overall System Accuracy, several sources of error are involved in the overall error, including the needle pose estimation error, the ultrasound calibration error, the camera calibration error and the ultrasound segmentation error. Because of the relatively poor resolution of the ultrasound, a fairly large portion of the overall error can be attributed to the ultrasound segmentation error. The segmentation error affects the accuracy of the system differently depending on various parameters such as depth, needle tilt angle, needle yaw angle and number of edge points, which was discussed in this article. The bias in Figure 11b can be partly attributed to calibration error, which could be the result of the two-step calibration procedure using a mirror. The calibration accuracy may be improved by acquiring more images for calibration.

Under Finding the Centerline and Fine-Tuning, the centerline was found by taking the center of the clusters of marker edge points. This assumes that the points are at least symmetrically and homogeneously distributed from side to side of the needle. To investigate whether the centerline estimation might be biased because of this first, we note that regardless of the light conditions from side to side of the needle, when considering any given line approximately along the needle, there is a difference in the intensity of the pixels between the dark marking part and the light part. For each line, one candidate edge point is stored on the edge of this transition. In

fact, because the local derivative is taken in the needle's axial direction, the light changes along the side-to-side of the needle will not affect the segmentation procedure as much. In fact, if enough numbers of random lines are considered, candidate edge points should be found along the entire side-to-side direction, as illustrated in Figure 5, and an accurate estimation of the centerline would be found.

There may still be a bias, however, if the lighting conditions remove features from one side of the needle more than the other side. The error will be less than the diameter of the needle.

To provide enough illumination and to robustly control the lighting conditions, one idea is to attach an infrared light source next to the camera. Invisible infrared light will not interfere with most of the routine procedures in the operating room, although it is visible by the camera. An illumination source will minimize most of the issues with lighting conditions.

The global setup or the human interface to the guiding system can be similar to existing commercial systems such as that of Stolka et al. (2014b).

CONCLUSIONS

Many needle intervention procedures are performed using ultrasound guidance because it is a flexible, cost-effective and available intra-operative imaging modality. In a needle insertion procedure with ultrasound guidance,

real-time calculation and visualization of the needle trajectory can help to guide the choice of puncture site and needle angle to reach the target depicted in the ultrasound image. In this article, we reported that not only it is feasible to calculate the needle trajectory with a single camera mounted directly on the ultrasound transducer by using the needle markings, but also higher accuracy (0.94 ± 0.46 mm) can be achieved compared with other similar transducer-mounted trackers.

As mentioned in the Introduction, the accuracy of existing solutions ranges from 2.6 ± 1.7 to 6.9 ± 5.1 mm, and in the previous version of our approach, accuracy was 3.0 ± 2.6 mm. Note that direct comparison of methods should be done with caution because different cameras and/or ultrasound transducers were used. The improvement over our previous work was, in fact, due to a more accurate and robust segmentation method, a more accurate ultrasound calibration, a generalized closed-form solution and a higher-quality camera. Moreover, note that in tracking systems that use stereo vision, there are other sources of error such as errors in extrinsic camera parameters (stereo calibration) and errors in image segmentation and stereo matching procedures (Chan et al. 2005). Also, in a transducer-mounted stereo tracking system, practical constraints limit the maximum distance between the stereo cameras, which leads to lower depth resolution.

Our proposed method provides a practical and efficient tracking solution that avoids some of the drawbacks of magnetic and external optical trackers. Moreover, our proposed tracking system is inexpensive, real time and easy to use. The proposed automatic feature extraction algorithm is accurate, robust and fast, and the closed-form method for pose estimation allows for rapid and accurate needle tracking.

One of the limitations of the proposed system is that it requires markings on the surface of the needle. A checkerboard marker can be attached to the hub of the needle if it does not have such markings. Moreover, unless tracking the needle continuously, it is not possible to locate the position of the tip once it is inserted into the tissue, as only the line equation is determined.

In the needle tracking system, it is desirable that the camera be freely rotated to accommodate both in-plane and out-of-plane needle insertions. Ultrasound calibration requires a special setup and can be time consuming, so here we proposed using a fixed marker on the transducer and holding the transducer in front of a mirror for a quick recalibration. However, we found that this approach can reduce the accuracy of the calibration. This recalibration procedure can be eliminated if the camera is tracked using a mechanical encoder to record its rotation in real time.

The next step is to investigate efficacy of the guidance system in clinical use, starting with epidural anesthesia.

REFERENCES

Abolhassani N, Patel R, Moallem M. Needle insertion into soft tissue: A survey. Med Eng Phys 2007;29:413–431.

Anim-Somuah M, Smyth R, Howell C. Epidural versus non-epidural or no analgesia in labour. Cochrane Database Syst Rev 2005;CD000331.

Bartynski WS, Grahovac SZ, Rothfus WE. Incorrect needle position during lumbar epidural steroid administration: Inaccuracy of loss of air pressure resistance and requirement of fluoroscopy and epidurography during needle insertion. Am J Neuroradiol 2005;26: 502–505.

Bernards CM, McDonald SB, Salinas FV. A practical approach to regional anesthesia. Philadelphia: Lippincott Williams & Wilkins; 2009.

Boctor EM, Choti MA, Burdette EC, Webster RJ III. Three-dimensional ultrasound-guided robotic needle placement: An experimental evaluation. Int J Med Robot 2008;4:180–191.

Bouguet JY. Visual methods for three-dimensional modeling. PhD thesis. Pasadena, CA, USA: California Institute of Technology; 1999.

Chan C, Lam F, Rohling R. A needle tracking device for ultrasound guided percutaneous procedures. Ultrasound Med Biol 2005;31: 1469–1483.

Collet A, Berenson D, Srinivasa SS, Ferguson D. Object recognition and full pose registration from a single image for robotic manipulation. Kobe: IEEE Press; 2009. p. 3534–3541.

Gonzalez RC, Woods RE, Eddins SL. Digital image processing using MATLAB. Upper Saddle River, NJ: Pearson Prentice Hall; 2004.

Haralick R, Lee D, Ottenburg K, Nolle M. Analysis and solutions of the three point perspective pose estimation problem. Proc IEEE Conf Computer Vision Pattern Recog 1991;598:592.

Hastie T, Tibshirani R, Friedman J, Hastie T, Friedman J, Tibshirani R. The elements of statistical learning, 2. Berlin/Heidelberg: Springer; 2009.

Holoborodko P. Smooth noise robust differentiators, 2008. www.holoborodko.com/pavel/numerical-methods/numerical-derivative/smooth-low-noise-differentiators/.

Khosravi S, Rohling R, Lawrence P. One-step needle pose estimation for ultrasound guided biopsies. Proc Annu Int Conf IEEE Eng Med Biol Soc 2007;2007:3343–3346.

Kumar RK, Ilie A, Frahm JM, Pollefeys M. Simple calibration of non-overlapping cameras with a mirror. Proc IEEE Conf Computer Vision Pattern Recog 2008;1–7.

Lowe DG. Distinctive image features from Scale-Invariant keypoints. Int J Comput Vis 2004;60:91110.

Lucchese L. Closed-form pose estimation from metric rectification of coplanar points. Proc IEEE Conf Vision Image Signal Process 2006;153:364–378.

Luhmann T. Precision potential of photogrammetric 6DOF pose estimation with a single camera. ISPRS J Photogramm Remote Sensing 2009;64:275–284.

Mercier L, Lang T, Lindseth F, Collins DL. A review of calibration techniques for freehand 3-D ultrasound systems. Ultrasound Med Biology 2005;31:449–471.

Najafi M, Afsham N, Abolmaesumi P, Rohling R. A closed-form differential formulation for ultrasound spatial calibration: Multi-wedge phantom. Ultrasound Med Biol 2014;40:2231–2243.

Najafi M, Rohling R. Single camera closed-form real-time needle trajectory tracking for ultrasound. Proc SPIE 2011;79641:79641F.

Rahbar K, Pourreza HR. Inside looking out camera pose estimation for virtual studio. Graph Models 2008;70:57–75.

Shi F, Zhang X, Liu Y. A new method of camera pose estimation using 2D–3D corner correspondence. Pattern Recog Lett 2004;25: 1155–1163.

Stolka P, Foroughi P, Rendina M, Weiss C, Hager G, Boctor E. Needle guidance using handheld stereo vision and projection for ultrasound-based interventions. In: Golland P, Hata N, Barillot C, Hornegger J, Howe R, (eds). Medical Image Computing and Computer-Assisted Intervention MICCAI 2014. Lecture Notes Computer Sci 2014a; 8674;. p. 684–691.

Stolka PJ, Foroughi P, Rendina M, Weiss CR, Hager GD, Boctor EM. Needle guidance using handheld stereo vision and projection for ultrasound-based interventions. In: Golland P, Hata N, Barillot C, Hornegger J, Howe R, (eds). Medical Image Computing and Computer-Assisted Intervention–MICCAI 2014. Lecture Notes Computer Sci 2014b;8674;. p. 684–691.

Wang XL, Stolka PJ, Boctor E, Hager G, Choti M. The kinect as an interventional tracking system. Proc SPIE 2012;83160U.

Zhang Z. Microsoft kinect sensor and its effect. IEEE MultiMedia 2012; 19:4–10.